

MDPI

Article

# Mixing Time Prediction in a Ladle Furnace

Xipeng Guo <sup>1</sup>, Yun Liu <sup>2</sup>, Yasmeen Jojo-Cunningham <sup>2</sup>, Armin Silaen <sup>1</sup>, Nicholas Walla <sup>1</sup> and Chenn Zhou <sup>1,\*</sup>

- Center for Innovation through Visualization and Simulation (CIVS), Purdue University Northwest, Hammond, IN 46323, USA; guo468@pnw.edu (X.G.); njwalla@pnw.edu (N.W.)
- Department of Mechanical and Civil Engineering, Purdue University Northwest, Hammond, IN 46323, USA; liu739@pnw.edu (Y.L.); yjojocun@pnw.edu (Y.J.-C.)
- \* Correspondence: czhou@pnw.edu

**Abstract:** This paper presents a study on the effectiveness of two turbulence models, the large eddy simulation (LES) model and the k- $\varepsilon$  turbulence model, in predicting mixing time within a ladle furnace using the computational fluid dynamics (CFD) technique. The CFD model was developed based on a downscaled water ladle from an industrial ladle. Corresponding experiments were conducted to provide insights into the flow field, which were used for the validation of CFD simulations. The correlation between the flow structure and turbulence kinetic energy in relation to mixing time was investigated. Flow field results indicated that both turbulence models aligned well with time-averaged velocity data from the experiments. However, the LES model not only offered a closer match in magnitude but also provided a more detailed representation of turbulence eddies. With respect to predicting mixing time, increased flow rates resulted in extended mixing times in both turbulence models. However, the LES model consistently projected longer mixing times due to its capability to capture a more intricate distribution of turbulence eddies.

Keywords: multiphase flow; turbulence; ladle metallurgy; shake-the-box; mixing time

#### 1. Introduction

Steel plays a vital role in our society and has significantly shaped our daily lives in various aspects, including infrastructure, transportation, manufacturing, energy, and so on. To produce high-quality steel, the ladle plays a significant role in the process as it facilitates processes such as steel property and temperature homogenization, inclusion removal, degassing, and desulfurization [1]. All these processes heavily rely on the mixing of molten steel, with gas injection from the bottom porous plug serving as the source of introducing momentum. To assess the mixing process in various ladles, mixing time is a crucial parameter. Mixing time signifies the duration needed for a solute-containing fluid upon introduction into a mixing vessel with solute-free fluid to uniformly disperse throughout the entire system up to a predetermined level of consistency. Typically, this consistency level is set at 95 percent of the ultimate concentration at all measurement points [2]. Two widely accepted transportation mechanisms that influence the mixing time are convective flow and turbulence diffusion [3]. The significant flow circulation stemming from the predominant upstream gas plume injection illustrates convective flow, whereas the dissipation of turbulence kinetic energy gives rise to turbulence diffusion. In this context, it is important to explore the impact of the main flow structure and turbulence kinetic energy on the mixing time. Numerous researchers have studied various variables that influence mixing time, including flow rate [4–7], ladle dimensions [8], plug arrangement [9–12], properties and thickness of the slag layer [13,14], and tracer location [15]. While some researchers argue that mixing time is not influenced by tracer location and release amount as long as homogeneity of 99.5% is achieved [3], this condition is often too extreme. Most studies suggest that with a homogeneity of 95%, mixing time is significantly impacted by



Citation: Guo, X.; Liu, Y.; Jojo-Cunningham, Y.; Silaen, A.; Walla, N.; Zhou, C. Mixing Time Prediction in a Ladle Furnace. *Metals* **2024**, *14*, 518. https://doi.org/10.3390/ met14050518

Received: 3 April 2024 Revised: 24 April 2024 Accepted: 27 April 2024 Published: 29 April 2024



Copyright: © 2024 by the authors. Licensee MDPI, Basel, Switzerland. This article is an open access article distributed under the terms and conditions of the Creative Commons Attribution (CC BY) license (https://creativecommons.org/licenses/by/4.0/).

Metals **2024**, 14, 518 2 of 17

tracer location and monitoring location [15,16], which is attributed to flow structure differences. This curiosity also extends to how mixing time might be influenced by turbulence models in simulations. The existing turbulence models struggle to resolve the detailed turbulence eddies and their dissipation, leading to variations and discrepancies in simulation results. This discrepancy is particularly clear in the two extensively used turbulence models for ladle furnace simulations: the k-epsilon (k- $\epsilon$ ) model and the large eddy simulation (LES) model. The k-ε model is one of the most popular Reynolds-averaged Navier-Stokes turbulence (RANS) models in ladle furnace simulation. It offers computational efficiency and practicality for industrial simulations, providing time-averaged insights into turbulent flows. However, it introduces potential inaccuracies due to its oversimplifications, struggles with complex flows, and lacks precision in capturing small-scale eddies. LES is a much more advanced turbulence model, which provides better accuracy in simulating turbulent flows and resolving large flow scales while modeling smaller ones. Its ability to resolve detailed flow features makes LES suitable for complex and unsteady flows [17]. However, its computational demands are high, limiting its use for practical engineering applications compared to less accurate turbulence models.

The objective of this study is to numerically simulate water ladle models with the k- $\epsilon$  and large eddy simulation (LES) turbulence models and to analyze flow structure and its impact on mixing time. The aim is to provide guidelines for utilizing these models in predicting ladle mixing time, ultimately leading to improved ladle design and operational conditions. The study also encompasses a volumetric flow measurement on a water ladle model using particle tracking velocimetry and the shake-the-box system.

#### 2. Present Work

In this study, a 0.02794 scaled cylindrical water ladle model with a diameter of 0.07 m and a liquid height of 0.084 m was utilized in both the numerical simulation and experiment. During the experiment, instead of water, a sodium iodide solution was utilized to match the refractive index of the container, thereby mitigating particle image distortion. The sodium iodide solution was prepared by dissolving sodium iodide powder in distilled water [18]. For simplicity, we will refer to it as a 'water ladle', though it specifically denotes a ladle containing the sodium iodide solution. To scale down the model from a full-sized industrial ladle, dynamic similarity analysis was carried out by a comparison of the Froude number and Reynolds number between the prototype and the model. However, achieving dynamic and geometric similarities between the prototype and model proved to be exceedingly challenging [19]. The Reynolds number is the ratio of inertial force to viscous force. Given that the Reynolds number was very high in both the prototype and the downscaled model, exceeding a magnitude of 10<sup>5</sup>, the influence of inertial force was significantly more pronounced compared to viscous force. Therefore, further attention was given to the Froude number [20]:

$$Fr = \frac{U_p^2}{gH} \tag{1}$$

Here,  $U_P$  represents the plume velocity, which can be calculated as follows [20]:

$$U_P = 3.1Q^{\frac{1}{3}}H^{\frac{1}{4}}R^{-0.58} \tag{2}$$

The downscaled flow rate can be calculated from Mazumdar's [21] work:

$$Q_M^{STP} = \lambda^{2.5} Q_P^{TP} \tag{3}$$

Here,  $Q_M$  is the flow rate in the downscaled model, while  $Q_P$  represents the flow rate in the full-scale ladle.  $\lambda$  is the scaling factor and is equal to 0.02794. In a real ladle furnace, the inert gas bubbles injected at the bottom of the ladle will be heated by the molten steel

Metals **2024**, 14, 518 3 of 17

as they ascend. Therefore, the correction for pressure and temperature should be taken into consideration [6,20,22], and the flow rate should be reformulated as follows:

$$Q_M^{STP} = 3.45\lambda^{2.5} Q_P^{STP} \tag{4}$$

The parameters of the prototype steel ladle and the downscaled water ladle are listed in Table 1. The comparison of the two dimensionless numbers in both the prototype and the downscaled water ladle is presented in Table 2. From Table 2, we can see that the Froude numbers in the model and prototype are very similar, which means that the physics of the plume in the prototype can be well reproduced in the water ladle. Regarding the Reynolds number, as mentioned before, although it is two magnitudes less in the water ladle than in the prototype, it is still greater than the turbulence threshold, meaning that turbulent flow is maintained in the water ladle.

Prototype—Steel Ladle Model—Water Ladle Ladle diameter 2.5 m Tank diameter 0.070 m0.084 m Steel height 3 m Solution height Steel density  $6795 \text{ kg/m}^3$ Solution density  $1793 \text{ kg/m}^3$ 0.002 Pa.s 0.006 Pa.s Steel viscosity Solution viscosity Surface tension—steel/argon 1.82 N/m Surface tension—solution/air 0.073 N/m

**Table 1.** Parameters of the prototype and the downscaled water ladle.

Table 2. Reynolds and Froude numbers of the prototype and downscaled water ladle.

Prototype—Steel Ladle			Model—Water Ladle		
Flow Rate	Reynolds Number	Froude Number	Flow Rate (20 $^{\circ}$ C)	Reynolds Number	Froude Number
208.18 NL/min	2,780,260	0.0228	0.10 L/min	11,575	0.0232

## 2.1. Mathematical Model

## 2.1.1. Assumptions and Considerations in Modeling

During the modeling process, a series of three-dimensional, transient, multiphase, turbulent flow simulations of the scaled water ladle model were conducted. The following assumptions and considerations were employed to facilitate these simulations:

- Solution and the air at the top were considered continuous phases, while the air bubbles injected from the bottom were treated as discrete phases.
- The flow was assumed to be fully turbulent.
- The experiment operated at a room temperature of 20 °C, and thus, the corresponding simulation was assumed to be isothermal. This implied that the density of the gas bubble responded solely to a change in pressure.
- The air bubbles were removed when the volume of air in the mesh cell exceeded 0.9.
- To study the mixing efficiency in the ladle, we employed the tracer method [6]. The
  properties of the tracer were assumed to be identical to those of the solution in the
  ladle. The coupling between the tracer species and solution was one-way, meaning
  that the movement did not affect the motion of the solution.

## 2.1.2. Governing Equations

There are three commonly utilized numerical simulation approaches to modelling ladle systems: 1. volume of fluid (VOF) multiphase model; 2. Eulerian multiphase model; and 3. VOF model coupling with discrete phase model (DPM). In the first category, both fluid and bubble are modeled as continuum phases, but only one set of equations of continuity and momentum is solved. Under this scheme, the bubble plume is modeled as a jetting regime

Metals **2024**, 14, 518 4 of 17

instead of individual particles [20]. Moreover, the forces acting on bubbles are neglected. Although the VOF model is renowned for its ability to track interfaces between different phases, its stability, and its relatively lower computational resource cost, the limitations of bubble simulation have led to the gradual abandonment of using a single VOF model. For the second method, a single Eulerian multiphase model can solve the transportation equations for each phase, which allows the user to include the effects of forces such as virtual mass force, pressure gradient force, drag force, turbulence dispersion force, etc. on bubble motions and the fluid flow. In a more advanced Eulerian model scheme, the population balance model (PBM) is further included to track the bubble coalescence and breakup [23,24]. However, because of the comprehensiveness and complexity of the model, the convergence of the Eulerian multiphase model has difficulties converging [25]. There are no studies showing the possibility of using the Eulerian multiphase model to simulate both steel and slag at the same time. To consider immiscible liquid interfaces and bubble behavior simultaneously, the third method was proposed. Under this scheme, a sharp interface can be tracked using the VOF model, and the bubble is modeled as a discrete phase. The force acting on bubbles, as mentioned before, can be added to each bubble, and the bubble motion is governed by Newton's second law. In summary, the VOF-DPM scheme best aligns with the objective of this study and was thus utilized.

Mass conservation can be described as follows:

$$\frac{\partial \rho}{\partial t} + \nabla \cdot \left( \rho \overrightarrow{u} \right) = 0 \tag{5}$$

Here,  $\overrightarrow{u}$  is the velocity of the continuum phase, and  $\rho$  is the fluid density. The momentum equation can be described as follows:

$$\frac{\partial}{\partial t} \left( \rho \overrightarrow{u} \right) + \nabla \cdot \rho \overrightarrow{u} \overrightarrow{u} = -\nabla p + \nabla \cdot \left[ \mu \left( \nabla \overrightarrow{u} + \overrightarrow{u}^T \right) \right] + \rho \overrightarrow{g} + \overrightarrow{F}_b$$
 (6)

Here,  $\overrightarrow{g}$  is local gravity acceleration,  $\mu$  is effective viscosity,  $\overrightarrow{u}$  is the velocity of the continuum phase,  $\rho$  is fluid density, and  $F_h$  is the force from the bubble.

The volume of fluid (VOF) model is particularly considered when calculating interface behavior between two or more immiscible fluids, making it a popular choice for simulating refining ladles. In this study, the VOF model was used to track the air/water interface. The continuity equation of the VOF model is given below:

$$\frac{\partial \alpha_i}{\partial t} + \overrightarrow{v} \cdot \nabla \alpha_i = 0 \tag{7}$$

$$\sum \alpha_i = 1 \tag{8}$$

The subscript "i" represents individual substances within the simulation, with the constraint that the sum of all the volume fractions is equal to one. Furthermore, it is important to note that the density and viscosity of the mixture depend on the volume fraction of each substance. For the bubbles injected from the bottom of the tank, they were treated as a discrete phase and were simulated using the discrete phase model (DPM). During this process, the behavior of the bubbles, including coalescence and breakup, is contingent on the local turbulent flow conditions. The motion of these discrete particles is governed by Newton's second law, which can be described as follows:

$$\frac{d\overrightarrow{u}_p}{dt} = F_D\left(\overrightarrow{u} - \overrightarrow{u}_p\right) + \frac{\overrightarrow{g}\left(\rho_p - \rho\right)}{\rho_p} + \overrightarrow{F}_{VM} + \overrightarrow{F}_{pressure}$$
(9)

Here,  $F_D(\overrightarrow{u} - \overrightarrow{u}_p)$  is the drag force per unit particle mass,  $\overrightarrow{u}$  is the continuum phase velocity, and  $\overrightarrow{u}_p$  is the bubble particle velocity.  $F_D$  is written as follows:

Metals **2024**, 14, 518 5 of 17

$$F_D = \frac{18\mu C_D R_e}{24\rho_p d_p^2} \tag{10}$$

The initial bubble diameter is assumed to be 0.003 m, which is the same as the inlet diameter. Bubble coalescence and breakup are fundamental processes in fluid dynamics and multiphase flow systems that involve the combination of two or more bubbles into a single, larger bubble (coalescence) and the division of a bubble into smaller bubbles (breakup). During the process, the bubble diameter will change, resulting in a change in the subsequent force balance. Here, the major assumption is that at every location within the fluid flow, there is an equilibrium bubble size related to both the bubble properties and the surrounding fluid flow conditions [26,27]. All the bubbles tend to coalesce or break up to reach this equilibrium diameter. The time it takes for a bubble to change its size can be referred to as the relaxation time.

The equilibrium diameter of the bubble can be calculated as follows:

$$d_b^{eq} = C_{b1} * \alpha_b^{0.5} \frac{\left(\frac{\sigma}{\rho}\right)^{0.6}}{\varepsilon^{0.4}} \left(\frac{\mu_b}{\mu}\right)^{0.25} + C_{b2}$$
 (11)

where  $\varepsilon$  is the dissipation of turbulent kinetic energy,  $\mu_b$  is the viscosity of the bubble phase,  $\sigma$  is the surface tension between bubbles and the ambient fluid, and  $\alpha_b$  is the bubble void fraction.  $C_{b1}$  is a dimensionless constant, while  $C_{b2}$  refers to the minimum bubble size, as described by Cloete et al. [27].  $C_{b1} = 4$  and  $C_{b2} = 0.0001$ .

The relaxation timescale can be expressed as follows:

$$\tau_{rel} = \begin{cases} \tau_B, & \text{if } d_b > d_b^{eq} \\ \tau_C, & \text{if } d_b < d_b^{eq} \end{cases}$$
 (12)

$$\tau_{rel} = |\tau_{rel}, \tau_K|_{max} \tag{13}$$

Here,  $\tau_B$  and  $\tau_C$  represent the timescales of breakup and coalescence, respectively. If the instantaneous bubble size is greater than the equilibrium size, it tends to break up; conversely, if it is smaller, it tends to coalesce. The relaxation time is constrained by the turbulent microscale. The turbulent microscale is given as follows:

$$\tau_K = 6\sqrt{\frac{v}{\epsilon}} \tag{14}$$

This is defined as 6 times the Kolmogorov timescale. Here, v is the kinematic viscosity of the fluid.

A bubble breaks up when the turbulent shear forces of the turbulence eddy are stronger than the surface tension forces of the bubble [28,29]. Large eddies, which are significantly bigger than the bubble, do not lead to breakup but instead cause the bubble to move. Similarly, very small eddies do not contribute to breakup because they are too small to exert sufficient shear force on the bubble. However, eddies that are roughly the same size as the bubble can induce a breakup. Therefore, the breakup timescale is defined as the dissipation timescale of an eddy that is the same size as the trapped bubble. In terms of coalescence, it is modeled by calculating the chance of contact between two nearby bubbles in turbulence [26].

The breakup time scale  $\tau_B$  and coalescence time scale  $\tau_C$  can be calculated as follows:

$$\tau_B = d_b^{\frac{2}{3}} \varepsilon^{-\frac{1}{3}} \tag{15}$$

$$\tau_C = 2 \left[ \frac{\pi}{6} \frac{(1 - \alpha_b)}{\alpha_b} \right]^{\frac{1}{3}} \frac{d_b}{\sqrt{\frac{2}{3}k}} \sqrt{1 + St}$$
 (16)

Metals **2024**, 14, 518 6 of 17

$$St = \frac{\tau_b}{\tau_I} \tag{17}$$

$$\tau_b = \frac{\rho_b d_b^2}{18\mu} \tag{18}$$

$$\tau_L = \left(\frac{\nu}{\epsilon}\right)^{\frac{1}{2}} \tag{19}$$

The Stokes number can be defined as the relationship between the particle response time and the system response time [30–32]. If  $St \ll 1$ , the particle will follow the flow closely, while if  $St \gg 1$ , the particle will move independently. Coupled with the time scale and time step size, the change in bubble size can be calculated.

One main objective of this study was to evaluate the impact of different turbulence models on the prediction of flow patterns and mixing times. Two widely used turbulence models, the realizable k- $\epsilon$  turbulence model and the large eddy simulation (LES) model, were implemented in this study.

#### 2.2. Realizable k-ε Turbulence Model

The k- $\epsilon$  turbulence model falls under the category of the Reynolds-averaged Navier–Stokes (RANS) model. In particular, the realizable variant of this model, which is a refinement of the standard model, is of interest due to its improved capability to accurately predict the spreading rate of round jets. This model has gained extensive use in modern ladle simulations [32]. The transportation equation for the realizable k- $\epsilon$  turbulence model can be described as follows:

$$\frac{\partial}{\partial t}(\rho k) + \nabla \cdot \left(\rho k \overrightarrow{u}\right) = \nabla \cdot \left[\left(\mu + \frac{\mu_t}{\sigma_k}\right) \nabla k\right] + G_k + G_b - \rho \varepsilon \tag{20}$$

$$\frac{\partial}{\partial t}(\rho\varepsilon) + \nabla \cdot \left(\rho\varepsilon \overrightarrow{u}\right) = \nabla \cdot \left[\left(\mu + \frac{\mu_t}{\sigma_{\varepsilon}}\right)\nabla\varepsilon\right] + \rho C_1 S_{\varepsilon} - \rho C_2 \frac{\varepsilon^2}{k + \sqrt{\nu\varepsilon}} + C_{1\varepsilon} \frac{\varepsilon}{k} C_{3\varepsilon} C_b \quad (21)$$

Here,  $G_k$  and  $G_b$  are the turbulence kinetic energy resulting from the velocity gradient and buoyancy, respectively.  $\sigma_k$  and  $\sigma_{\varepsilon}$  are turbulence Prandtl numbers and equal to 1.0 and 1.2, respectively.

## 2.3. Large Eddy Simulation (LES) Turbulence Model

In this study, another turbulence model, the large eddy simulation (LES), was also implemented. In turbulent flows, a spectrum of eddies with various lengths and time scales exists. The largest eddies, typically on a scale similar to the characteristic length of the mean flow, such as shear layer thickness, play the most significant role. The dissipation of turbulence kinetic energy is primarily attributed to the smallest scales. The direct numerical simulation (DNS) approach theoretically has the potential to resolve the entire range of turbulent scales, but its practical application in ladle systems is limited by computational power. LES offers a compromised solution between DNS and RANS by directly resolving the larger eddies while modeling the smaller ones. Consequently, LES can be an intermediate solution regarding the proportion of resolved scales. However, the subgrid-scale (SGS) results from the filtering process are not known and need remodeling. Subgrid-scale turbulence models utilize the Boussinesq hypothesis [33], similar to the RANS models, to calculate the subgrid-scale turbulent stresses from the following equation:

$$\tau_{ij} - \frac{1}{3}\tau_{kk}\delta_{ij} = -2\mu_t \overline{S_{ij}} \tag{22}$$

Here,  $\mu_t$  is the subgrid-scale turbulence viscosity.  $\tau_{kk}$  is the isotropic component of the subgrid-scale stresses, which is not modeled but is included in the filtered static pressure term. The rate-of-strain tensor,  $\overline{S_{ij}}$ , for the resolved scale is defined as follows:

Metals **2024**, 14, 518 7 of 17

$$\overline{S_{ij}} = \frac{1}{2} \left( \nabla \overrightarrow{u} + \left( \nabla \overrightarrow{u} \right)^T \right)_{ij} \tag{23}$$

The Smagorinsky–Lilly model has been selected to calculate eddy viscosity. Eddy viscosity can be modeled as follows:

$$\mu_t = \rho L_s^2 |\overline{S}| \tag{24}$$

$$|\overline{S}| = \sqrt{2\overline{S_{ij}S_{ij}}} \tag{25}$$

$$L_s = \min(\kappa d, C_s \Delta) \tag{26}$$

Here,  $\kappa$  is the von Kármán constant set at 0.41, d is the distance to the closet wall,  $C_s$  is the Smagorinsky constant set at 0.1.  $L_s$  is the mixing length for the subgrid scale; it is also called the subgrid length scale.  $\Delta$  is the local mesh scale, which is calculated from mesh cell volume (V), as shown in the expression below:

$$\Delta = \sqrt[3]{V} \tag{27}$$

## 3. Computational Domain and Boundary Conditions

The computational domain is presented in Figure 1. The simulated tank's height was 0.1778 m, with additional dimensions detailed in Table 1. For boundary conditions, the side ladle wall and bottom were designated as no-slip walls, ensuring the fluid motion was constrained at these surfaces. Conversely, the top surface was designed as a pressure outlet with a gauge pressure of 0 Pascal, allowing fluid to exit freely. Furthermore, two circular surfaces were created on the bottom surface and defined as the locations of the bubble injection.

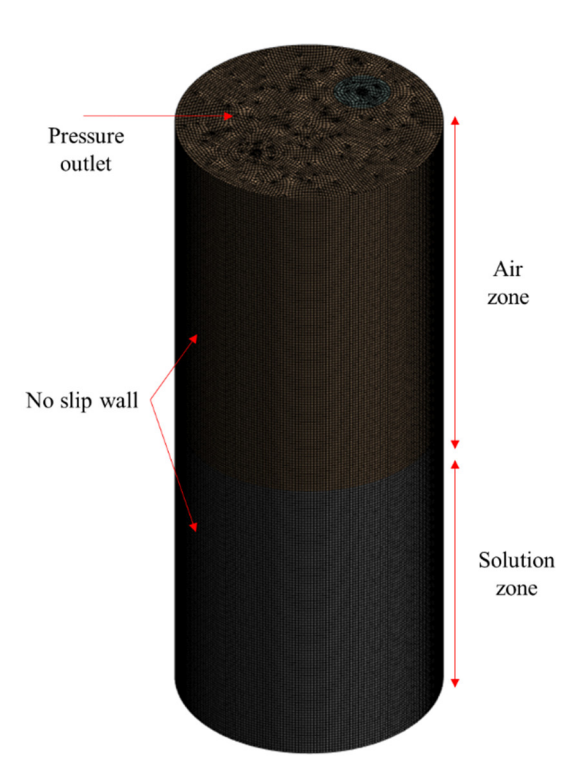


Figure 1. Mesh and boundary conditions of the computational domain.

#### 4. Simulation Procedure

The simulations were conducted using the commercial software ANSYS Fluent 2020 R1 (Canonsburg, PA, USA). The widely used SIMPLE scheme was applied in the simulations using the k- $\epsilon$  turbulence model. Additionally, customized scripts were used to model

Metals **2024**, 14, 518 8 of 17

bubble coalescence and breakup. To enhance accuracy, a second-order momentum scheme was utilized. The time step size was fixed at 0.002 s. The convergence criteria were set as requiring the residuals of all variables to be below 0.001 for convergence. In the case of the discrete phase model (DPM), it was employed to simulate the behavior of bubbles, with the simulation terminating the bubble trajectory once the air phase volume fraction exceeded 0.9. For the simulation of large eddy simulation (LES), the PISO scheme was chosen for pressure–velocity coupling with a constant time step of 0.002 s.

## 4.1. Experiment Measurements

As shown in Figure 2, during the experiment, a cylindrical container with an inner diameter of 70 mm was used to simulate and replicate the characteristics of a cylindrical ladle [34]. However, due to the curved surface of the cylindrical container, which would introduce significant particle image distortion from refraction, conventional flow field measurement methods, such as particle image velocimetry, and particle tracking velocimetry, cannot be directly implemented to measure the flow field. Therefore, this study adopted the refractive index matching method to counteract the effects of image distortion due to refraction. Additionally, to capture and film the particle images from four different perspectives, a four-camera particle tracking velocimetry system was strategically configured on a larger hexagon tank with six flat walls meticulously designed to accommodate the angle of imagining. This larger hexagon tank was designed to allow the cameras to film the flow inside the cylindrical tank, which was positioned at the center of the larger hexagon tank, with the cameras filming perpendicular to the flat walls. Both tanks were fabricated from plexiglass. To ensure optimal refractive index matching and thereby minimize image distortion, a sodium iodide solution was prepared and used to fill the tanks to a solution height of 0.084 m. Importantly, the refractive index of the sodium iodide solution closely aligns with that of plexiglass, ensuring minimum light refraction as the scatted light from the seeding particles traverses the curved plexiglass walls and the solution, eliminating particle image distortion when particle tracking velocimetry was employed.

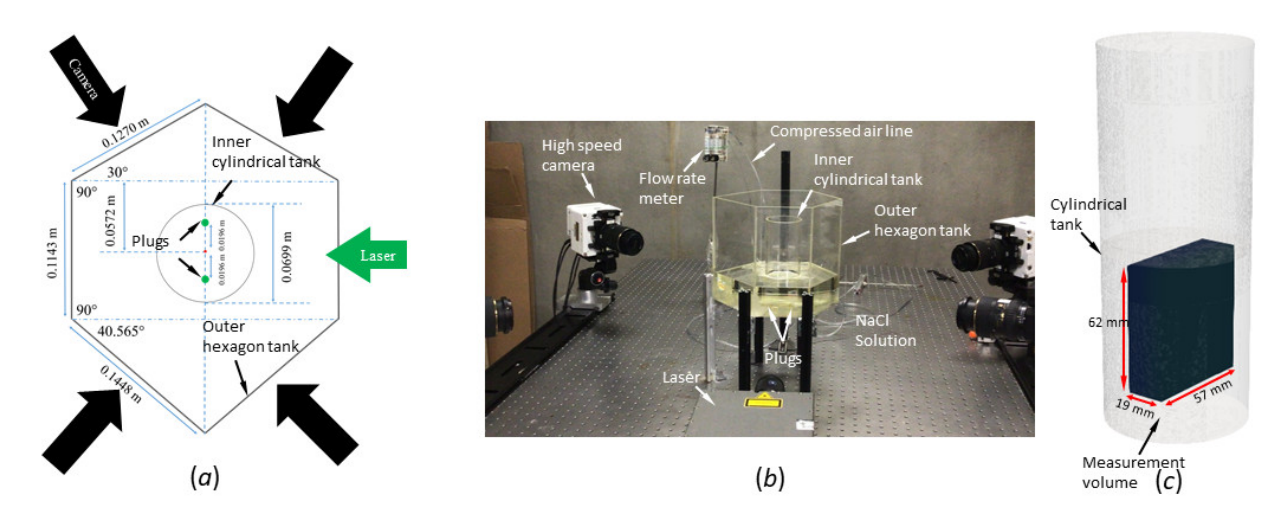


**Figure 2.** (a) Schematic of the water tank (top view); (b) water ladle setup in the experiment; (c) measured zone in the water tank. Adapted from Ref. [34].

#### Particle Tracking Velocimetry System

The shake-the-box system (Lavision, Gottingen, Germany) was implemented on the cylindrical water ladle model, which injected compressed air to stir the flow. To accurately track the intricate gas-stirred water flow within the water ladle model, hollow glass spheres with a diameter range of 8 to 12  $\mu$ m were used as seeding particles. To capture the seeding particles in the flow field and film the particle images, a high repetition rate laser (Photonics DM-30-527, Photonics Industries International Inc., Ronkonkoma, NY, USA) and four high-speed cameras (Phantom VEO 640, Vision Research Inc., Wayne, NJ, USA) were strategically

Metals **2024**, 14, 518 9 of 17

positioned on two sides of the experimental setup and utilized. Tokina Macro Lenses (Tokina USA, Huntington Beach, CA, USA) with a focal length of 100 mm and an aperture size of f = 4.5 were incorporated into the imaging system to facilitate capturing particle images within the flow field. To ensure optimal illumination and imaging, cylindrical optical lenses were added to the laser head, generating a 20 mm thick laser light that effectively penetrated and illuminated the inner cylindrical tank from the side. The sampling frequency of the images/laser was set at 100 Hz, with an image resolution of  $1024 \times 1024$  pixels maintained across all four high-speed cameras. This setup enabled the precise capture and subsequent analysis of the three-dimensional flow field within a volume domain measuring  $6 \times 6 \times 2$  cm. The software Davis 10 (LaVision, Gottingen, Germany) was employed for calibration, data collection, and velocity field construction. To achieve accurate calibration, a  $55 \times 55$  mm calibrated target was positioned within the sodium iodide solution, allowing for the acquisition of calibration images. Calibration was performed in Davis 10 using four images of the target. For enhanced accuracy in sub-pixel measurements and to facilitate volumetric flow field analysis, volume self-calibration was incorporated into the shake-thebox system. The shake-the-box algorithm (LaVision, Gottingen, Germany) was then used to carry out particle reconstruction/tracking by shaking the particle position by 1 voxel during the iterations. The culmination of these processes involves the reconstruction of the instantaneous volumetric velocity field through post-processing within Davis 10. This resulted in three  $15 \times 13 \times 5$  matrices, each representing volumetric velocities along the three dimensions with a spatial resolution of 4.7 mm/velocity vector. For a more in-depth understanding of the shake-the-box algorithm and its workings, please refer to Schanz et al. [35] and Novara et al. [36].

#### 5. Results and Discussion

#### 5.1. Mesh Sensitivity Study of the k- $\varepsilon$ Model

To ensure an accurate numerical simulation with a minimum mesh size, a comprehensive mesh sensitivity study was conducted. The objective was to minimize the impact of cell size and quality on the simulation outcomes. Therefore, three distinct meshes of varying sizes were tested to achieve this goal. Figure 3a illustrates three horizontal planes selected for comparing velocities across different meshes, extending from the bottom of the ladle to the water–air interface. For each plug, a constant gas flow rate of 0.1 LPM was utilized. Notably, the upper portion of the tank exhibited higher velocity compared to the lower region. Throughout the initial stages of the simulation, a pronounced surge in velocity was observed as the ascending bubble plume reached the height of the ladle. However, as the simulation progressed, the flow pattern transformed, resulting in a steady circulation in the ladle. This shift led to a downward flow, subsequently causing a reduction in the average velocity magnitude within the measurement planes. Eventually, the flow reached a quasi-steady state. The cell sizes for the coarse mesh, base mesh, and refined mesh were set to 0.001 m (0.7 million cells), 0.0008 m (1.4 million cells), and 0.0006 m (3.0 million cells), respectively. Figure 3b demonstrates that the differences among the three meshes were minimal. However, a noticeable distinction emerged between the results of the coarse mesh and the other two meshes, while the base mesh and the fine mesh had almost identical velocity distributions. The computational expense for the base mesh was 60% of that for the fine mesh. Therefore, the base mesh was selected for further analysis.

Metals 2024, 14, 518 10 of 17

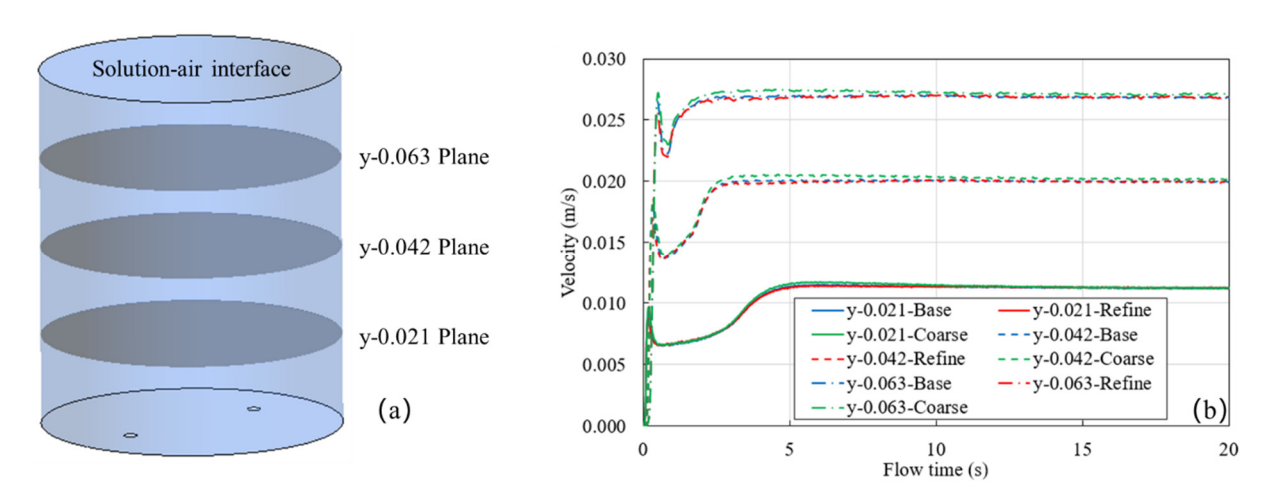


Figure 3. (a) Location of horizontal planes; (b) velocity on horizontal planes from different meshes.

## 5.2. Mesh Study of the LES Model

LES is widely acknowledged for its sensitivity to mesh size, as evident from Equation (17). A finer mesh generally yields more accurate results, albeit with higher computational costs. A methodology for evaluating LES results, introduced by Pope [31], involves defining the LES resolved index—a parameter computed using the following formulas:

$$\xi_k = \frac{k_{res}}{k_{tot}} = \frac{k_{res}}{k_{res} + k_{sgs}} \tag{28}$$

$$k_{res} = \frac{1}{2} \left( \overline{(u_1')^2} + \overline{(u_2')^2} + \overline{(u_3')^2} \right)$$
 (29)

$$k_{sgs} = \left(\frac{\mu_t}{\rho L_s}\right)^2 \tag{30}$$

Here,  $k_{res}$  stands for resolved turbulence kinetic energy, representing the kinetic energy resolved from cell level, while  $k_{sgs}$  signifies the turbulence kinetic energy contributed by eddies with a length scale too small to be resolved on a computational mesh [37]. The summation of  $k_{res}$  and  $k_{sgs}$  yields the total turbulence kinetic energy in the domain.  $u'_1$ ,  $u'_2$ , and  $u'_3$  are the velocity fluctuations in the x, y, and z directions.

The LES resolved index represents the ratio between Reynolds-averaged Navier-Stokes simulation (RANS, when  $\xi_k = 0$ ) and direct numerical simulation (DNS, when  $\xi_k = 1$ ). A larger ratio signifies a higher level of directly resolved turbulence. Pope recommends a threshold of 0.8, signifying 80% of the turbulence being resolved. For this study, the LES resolved index was applied, and the analysis was conducted across three mesh configurations. The cell dimensions for the LES coarse mesh, LES base mesh, and LES refined mesh were 0.0008 m (1.4 million cells), 0.0006 m (3.0 million cells), and 0.0004 m (6.0 million cells), respectively. The CPU hours required for each mesh to complete one full simulation (30 s) were 9216, 13,824, and 36,864 h. To visualize the resolved index within the solution zone, two vertical planes were selected, as depicted in Figure 4a. Figure 4b presents the LES resolved index on the vertical plane for the different meshes, with the blue region indicating an index below 0.8. As the cell size decreased, the percentage of resolved turbulence kinetic energy increased. The volume-averaged resolved index for each case was 0.87, 0.90, and 0.93, respectively. Considering that the LES coarse mesh already exceeded the 0.8 index threshold and given that the CPU hours needed for the LES coarse mesh were 66% and 25% of those required for the LES base mesh and LES fine mesh, respectively, it was deemed worthy of further investigation.

Metals **2024**, 14, 518 11 of 17

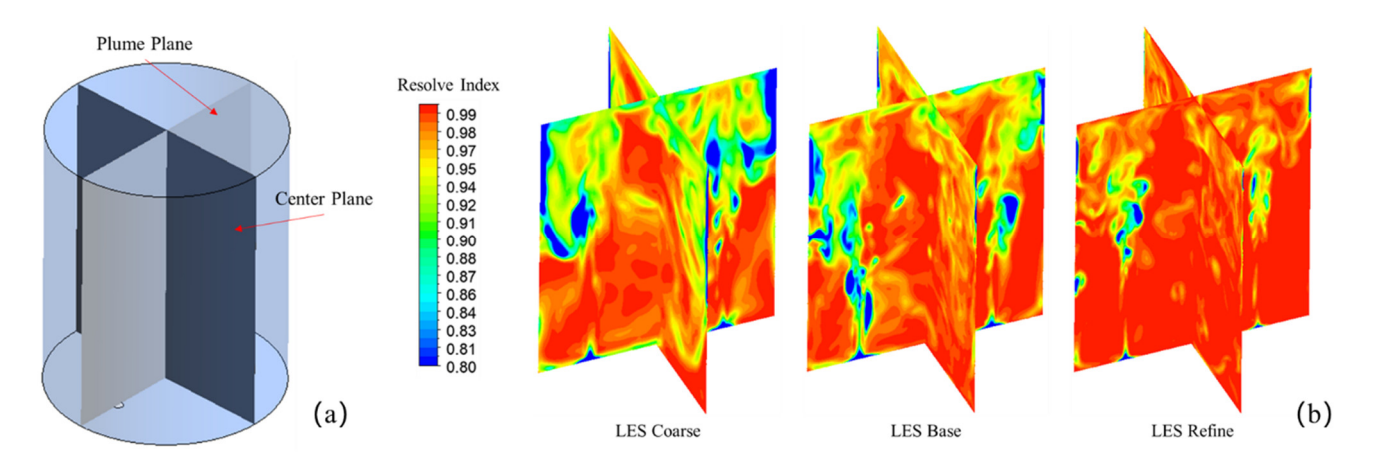


Figure 4. (a) Location of vertical planes; (b) LES resolve index on vertical planes from different meshes.

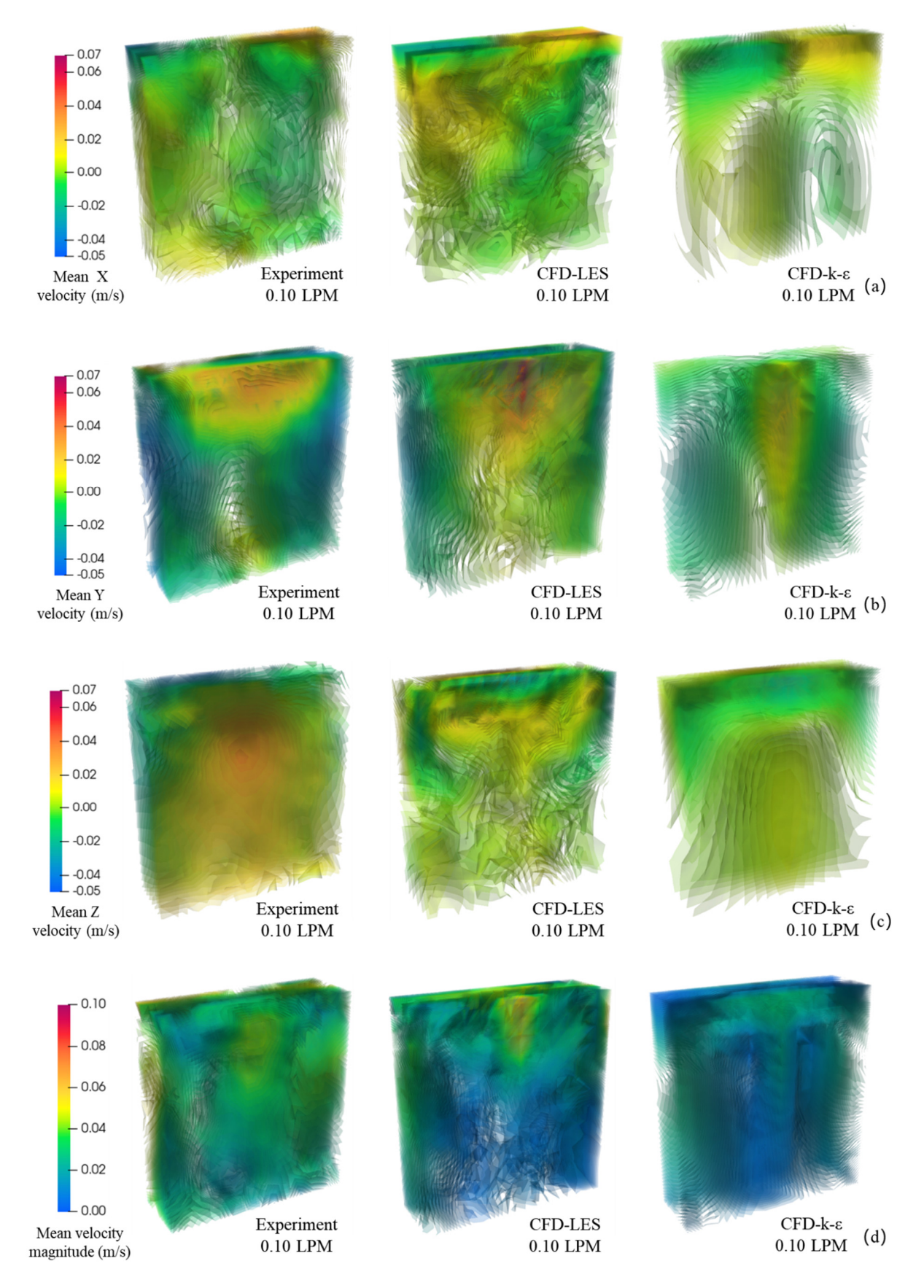
## 6. Flow Field Comparison between Experiment and CFD

Figure 5 presents comparisons of mean flow velocity components between experimental measurements and CFD simulations in the measured domain. In these figures, experimental results (first column) present time-averaged velocity data over a time duration of 20 s. Correspondingly, simulation results represent time-averaged values over a 10 s period following a 20 s flow run. For visualizing volumetric velocity distribution, the volumetric flow velocity field is displayed using 50 iso-surfaces of different velocity values (the surface is composed of points with equal velocity values). These iso-surfaces also provide insights into the distribution of the flow structure. Figure 5a demonstrates the distribution of mean flow velocity in the lateral direction (X direction). Experimental results revealed positive velocities in the upper right and lower left corners, contrasted by reverse velocities in the opposing positions. A similar trend was observed in CFD simulation results from both the LES and  $k-\varepsilon$  simulations. Figure 5b displays the distribution of mean velocity in the vertical direction (Y direction). Experimental observations highlighted elevated positive velocities in the upper center region, primarily due to the gas plume. Additionally, distant downward flows flanked both sides of the measurement area. In the LES simulation, the flow distribution closely resembled the experimental measurements. Conversely, the  $k-\varepsilon$  simulation indicated a more organized flow pattern, characterized by two primary circulations. Figure 5c,d showcase the distributions of mean velocity in the through thickness direction (Z direction) and mean velocity magnitude, respectively. Both the LES and k- $\varepsilon$  simulations captured the major flow characteristics that were observed in the experiment. However, neither CFD model could entirely replicate the experimental flow behavior. In the LES simulation, the magnitude aligned more closely with the experimental data, revealing finer flow structures, while the k-epsilon simulation yielded highly symmetric results.

For a more quantitative comparison between the experiment and simulation data, the measurement zone was subdivided into 13 planes along the x direction and 5 planes along the z direction, as shown in Figure 6.

Figure 7 displays the dimensionless plane-averaged mean velocity magnitude ( $|U|/\overline{|U|}$ ), where  $|\overline{U}|$  denotes the total mean velocity magnitude value of the entire domain. The average differences between the experiment and CFD-LES and CFD-k- $\varepsilon$  were 4.16% and 1.67%, respectively. From the results, the better prediction of velocity trend came from the result of the CFD-k- $\varepsilon$  model, which was due to the time-averaged nature of the RANS model. For the LES model, it needed more time to smooth out the trend. In general, the simulation results derived from both turbulence models (blue and green curves) aligned well with the experimental results.

Metals **2024**, *14*, 518



**Figure 5.** (a) Mean X velocity comparison between the experiment and CFD; (b) mean Y velocity comparison between the experiment and CFD; (c) mean Z velocity comparison between the experiment and CFD; (d) mean velocity magnitude comparison between the experiment and CFD.

Metals **2024**, 14, 518 13 of 17

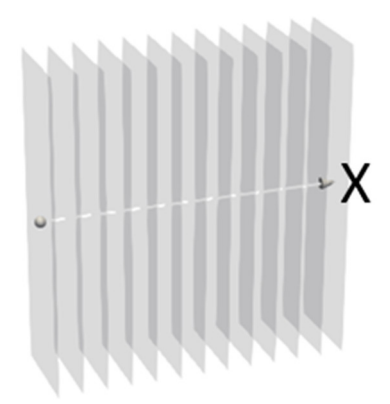


**Figure 6.** Measured zone sliced along the x direction.

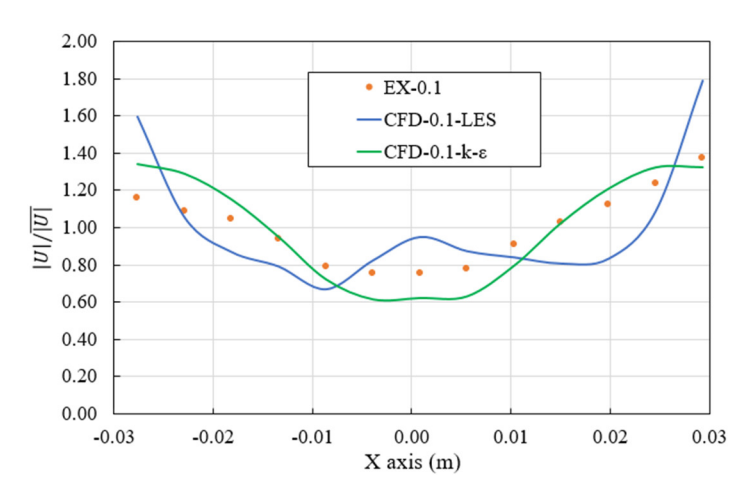


**Figure 7.** Dimensionless plane averaged velocity magnitude along the X axis.

## 7. Study of Mixing Time

The mixing time stands as a crucial parameter in evaluating ladle design and has garnered extensive attention in ladle CFD simulations [6,38,39]. In this study, our focus revolved around the exploration of mixing time based on the LES and  $k-\varepsilon$  turbulence models. To achieve this objective, six initial tracer sites were uniformly distributed within the ladle, as illustrated in Figure 8a. To capture historical mixing data, the tracer concentrations were recorded at 11 strategically selected locations, as shown in Figure 8b.

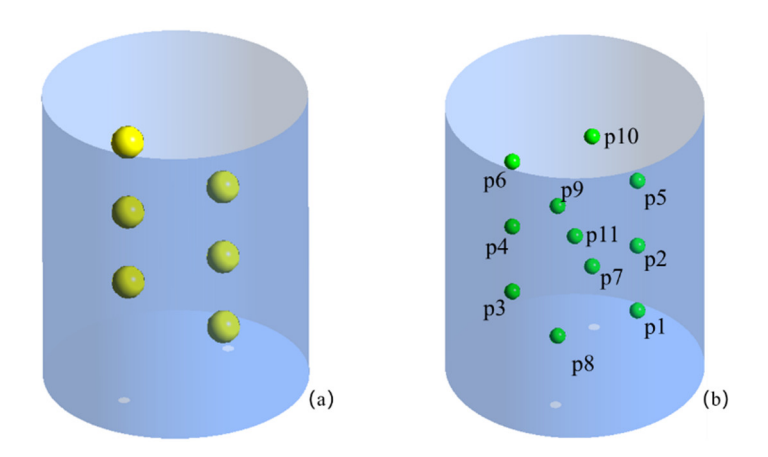


Figure 8. (a) Initial tracer locations; (b) monitor points in the ladle.

Metals **2024**, 14, 518 14 of 17

0.15 LPM

0.2 LPM

The simulation investigated three distinct flow rates: 0.10, 0.15, and 0.20 LPM. Within each flow rate scenario, two different turbulence models were employed, leading to a total of six cases. The configuration matrix for these cases is presented in Table 3.

Case	Flow Rate	Turbulence Model	Mixing Time
CFD-0.1-LES	0.1 LPM	LES	10.8 s
CFD-0.15-LES	0.15 LPM	LES	8.4 s
CFD-0.2-LES	0.2 LPM	LES	7.0 s
CFD-0.1-k-ε	0.1 LPM	Realizable k-ε	8.8 s

**Table 3.** Case matrix and mixing time.

CFD-0.15-k-ε

CFD-0.2-k-ε

Figure 9 provides a depiction of the species (tracer) mass fraction history for the LES 0.1 LPM case. It is evident that the species mass fraction starts high in proximity to the initial tracer sites and gradually diminishes as these points move farther away. However, over time, the species mass fraction for all points converges toward a uniform value. The mixing time is defined as the time required to achieve the mixing percentage ( $\alpha$ ) of 95% for all points. The mixing percentage can be computed using the following equation:

$$\alpha = 1 - \frac{\max(Y_i) - \min(Y_i)}{\max(Y_i)} \tag{31}$$

Realizable k-ε

Realizable k-ε

 $7.1 \mathrm{s}$ 

6.0 s

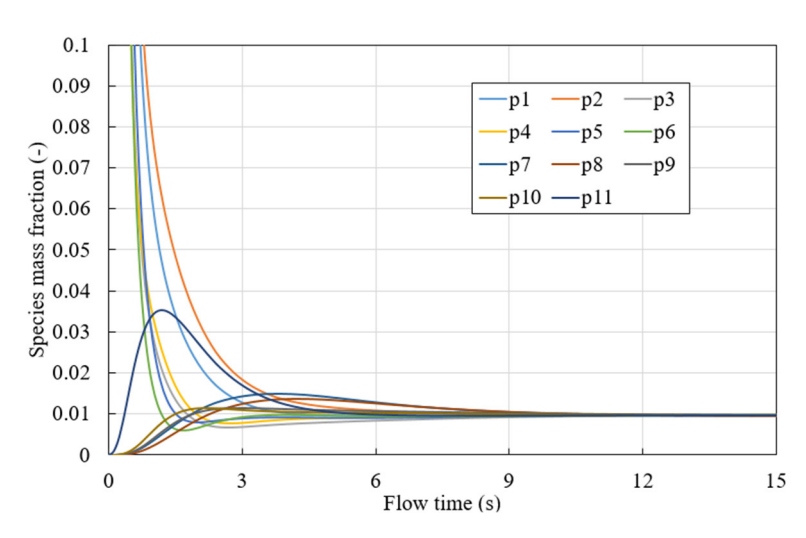


Figure 9. Change of species mass fraction in monitor points (LES 0.1 LPM).

Here,  $Y_i$  means species mass fraction at each monitor point.

Figure 10 presents the mixing percentage plotted against flow time for each case, and Table 3 records the mixing times for each case. For both turbulence models, the mixing time decreased as the flow rate increased. This trend can be partially attributed to the amplified flow velocities and turbulence kinetic energy, as evident in Figure 11. These factors resulted in heightened momentum, enabling species to traverse more rapidly and consequently achieve homogeneous mixing conditions more rapidly.

Moreover, it is evident that the mixing time computed by the LES model surpassed that of the k- $\epsilon$  model at equivalent flow rates, particularly within the lower flow rate range. Nonetheless, as the flow rate increased to 0.2 LPM, the volume-averaged turbulence kinetic energy from both models became nearly identical. This prompted further exploration into why the LES model exhibited longer mixing times. As noted by González-Bernal et al. [3],

Metals **2024**, *14*, 518

the fluid dynamics structure significantly influences mixing time. The presence of smaller eddies can lead to slower mixing, as species might become trapped within these eddies for extended periods. As shown in Figure 5, the flow field simulated by the LES model showed more unorganized small eddies. This phenomenon is also evident in Figure 10, where the mixing percentage line of the LES model might have decreased due to species being entrapped within eddies for prolonged durations.

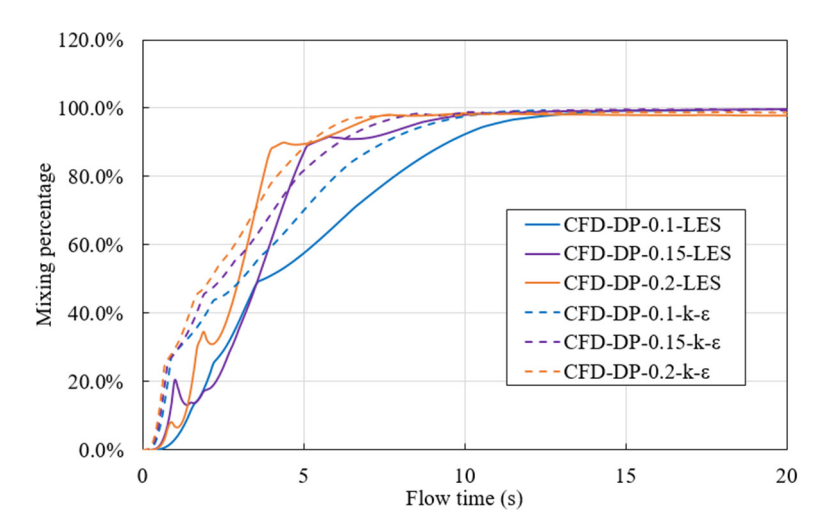


Figure 10. Mixing percentage of all cases.

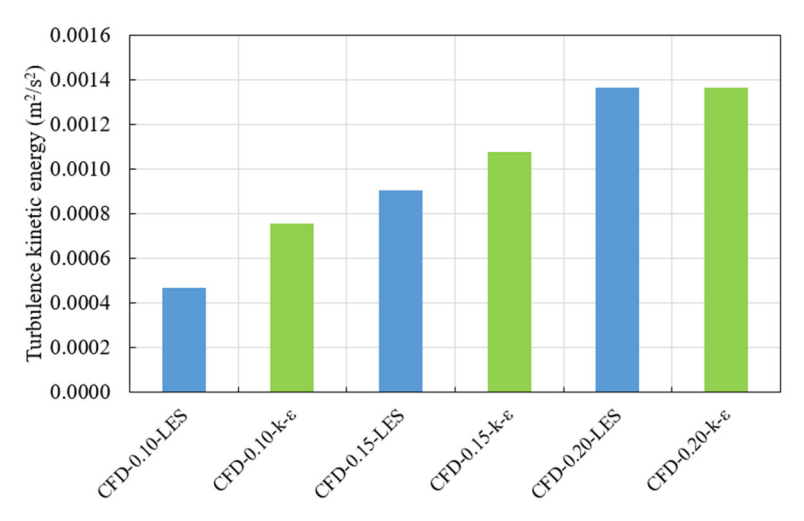


Figure 11. Averaged turbulence kinetic energy.

The findings provide a valuable insight, suggesting that when comparing mixing times, it is crucial to not only consider turbulence kinetic energy but also to conduct a comprehensive analysis of the fluid dynamic structure. This structure can significantly influence both process quality and productivity.

However, when focusing solely on studying the impact of different designs on mixing time, both the k- $\epsilon$  model and the LES model can be utilized. This is because, over time, the effects of small-scale turbulence will eventually be overshadowed by the main vortex. In other words, without delving into detailed analysis, both models are suitable for comparing mixing times. But for a detailed analysis of flow fields, mixing times, or other parameters, the LES model is recommended.

#### 8. Conclusions

In this paper, a three-dimensional flow measurement on the scaled water ladle was conducted. A scaled water ladle model was developed from an industry ladle. Two benchmark

Metals **2024**, *14*, 518

CFD simulations were developed for different flow rates and compared using two different turbulence models: the LES turbulence model and the k- $\epsilon$  turbulence model. The flow field was measured from the water ladle model and used to compare the results with CFD results. Mesh studies based on these turbulence models were also examined. The investigation focused on flow field, turbulence kinetic energy, and mixing time. The main findings from the study are as follows:

- 1. Two benchmark CFD simulations using the k- $\epsilon$  model and the LES model to study mixing time were conducted. A comprehensive mesh study, flow field analysis, and mixing time prediction were developed.
- 2. Both the LES model and the  $k-\varepsilon$  turbulence model could accurately predict the trend of fluid flow. However, the LES model exhibited a greater level of similarity in turbulence eddies and velocity magnitude when compared to experimental data.
- 3. For studying the impact of design differences on mixing time, both the k- $\epsilon$  and LES models are suitable, as the effects of small-scale turbulence diminish over time due to the main vortex. However, for detailed analysis of the flow field, mixing time, or other parameters, the LES model is preferred.

**Author Contributions:** Conceptualization, X.G. and Y.L.; methodology, X.G., L.Y, Y.J.-C., A.S. and N.W.; software, X.G.; validation, X.G., Y.L. and Y.J.-C.; investigation, X.G. and Y.L.; writing—original draft, X.G.; writing—review and editing, X.G., L.Y, Y.J.-C., A.S. and N.W.; supervision, C.Z.; project administration, C.Z.; funding acquisition, Y.L. and C.Z. All authors have read and agreed to the published version of the manuscript.

**Funding:** This work was supported in part by the National Science Foundation through its MRI program (CMMI-1919726) and GOALI program (CMMI-2113967). Support from all members of the Steel Manufacturing Simulation and Visualization Consortium (SMSVC) and the SMSVC Ladle Project Technical Committee is greatly acknowledged.

**Data Availability Statement:** The raw data supporting the conclusions of this article will be made available by the authors on request.

**Conflicts of Interest:** The authors declare no conflicts of interest.

#### References

- 1. Mishra, B. Steelmaking practices and their influence on properties. In *Metals Handbook Desk Edition*; ASM International: Materials Park, OH, USA, 1998; pp. 174–202.
- 2. Jardón-Pérez, L.E.; Amaro-Villeda, A.; González-Rivera, C.; Trápaga, G.; Conejo, A.N.; Ramírez-Argáez, M.A. Introducing the Planar Laser-Induced Fluorescence Technique (PLIF) to Measure Mixing Time in Gas-Stirred Ladles. *Met. Mater. Trans. B* **2019**, *50*, 2121–2133. [CrossRef]
- 3. González-Bernal, R.; Solorio-Diaz, G.; Ramos-Banderas, A.; Torres-Alonso, E.; Hernández-Bocanegra, C.A.; Zenit, R. Effect of the Fluid-Dynamic Structure on the Mixing Time of a Ladle Furnace. *Steel Res. Int.* **2017**, *89*, 1700281. [CrossRef]
- 4. Duan, H.; Zhang, L.; Thomas, B.G.; Conejo, A.N. Fluid flow, dissolution, and mixing phenomena in argon-stirred steel ladles. *Metall. Mater. Trans. B* **2018**, *49*, 2722–2743. [CrossRef]
- 5. Haiyan, T.; Xiaochen, G.; Guanghui, W.; Yong, W. Effect of Gas Blown Modes on Mixing Phenomena in a Bottom Stirring Ladle with Dual Plugs. *ISIJ Int.* **2016**, *56*, 2161–2170. [CrossRef]
- 6. Liu, Y.; Bai, H.; Liu, H.; Ersson, M.; Jönsson, P.G.; Gan, Y. Physical and Numerical Modelling on the Mixing Condition in a 50 t Ladle. *Metals* **2019**, *9*, 1136. [CrossRef]
- 7. Ramírez-Argáez, M.A.; Dutta, A.; Amaro-Villeda, A.; González-Rivera, C.; Conejo, A.N. A Novel Multiphase Methodology Simulating Three Phase Flows in a Steel Ladle. *Processes* **2019**, 7, 175. [CrossRef]
- 8. Mazumdar, D.; Guthrie, R.I.L. The Physical and Mathematical Modelling of Gas Stirred Ladle Systems. *ISIJ Int.* **1995**, *35*, 1–20. [CrossRef]
- 9. Liu, H.; Qi, Z.; Xu, M. Numerical Simulation of Fluid Flow and Interfacial Behavior in Three-phase Argon-Stirred Ladles with One Plug and Dual Plugs. *Steel Res. Int.* **2011**, *82*, 440–458. [CrossRef]
- 10. Tan, F.; He, Z.; Jin, S.; Pan, L.; Li, Y.; Li, B. Physical Modeling Evaluation on Refining Effects of Ladle with Different Purging Plug Designs. *Steel Res. Int.* **2020**, *91*, 1900606. [CrossRef]
- 11. Xing, L.; Xiao, W.; Bao, Y.; Wang, M.; Ai, X. Process optimization of bottom-blown argon for 130t ladle furnace. *Ironmak. Steelmak.* **2023**, *50*, 894–899. [CrossRef]
- 12. Akbari, M.; Safaei, B.; Zarei, T. Investigation of gas purging configuration in an industrial ladle by computational fluid dynamics. *Phys. Fluids* **2023**, *35*, 053334. [CrossRef]

Metals **2024**, 14, 518 17 of 17

13. Conejo, A.N.; Kitamura, S.; Maruoka, N.; Kim, S.-J. Effects of top layer, nozzle arrangement, and gas flow rate on mixing time in agitated ladles by bottom gas injection. *Metall. Mater. Trans. B Process Metall. Mater. Process. Sci.* **2013**, 44, 914–923. [CrossRef]

- Jardón-Pérez, L.E.; González-Morales, D.R.; Trápaga, G.; González-Rivera, C.; Ramírez-Argáez, M.A. Effect of Differentiated Injection Ratio, Gas Flow Rate, and Slag Thickness on Mixing Time and Open Eye Area in Gas-Stirred Ladle Assisted by Physical Modeling. Metals 2019, 9, 555. [CrossRef]
- 15. Herrera-Ortega, M.; Ramos-Banderas, J.; Hernández-Bocanegra, C.A.; Montes-Rodríguez, J.J. Effect of the Location of Tracer Addition in a Ladle on the Mixing Time through Physical and Numerical Modeling. *ISIJ Int.* **2021**, *61*, 2185–2192. [CrossRef]
- 16. Gajjar, P.; Haas, T.; Owusu, K.B.; Eickhoff, M.; Kowitwarangkul, P.; Pfeifer, H. Physical study of the impact of injector design on mixing, convection and turbulence in ladle metallurgy. *Eng. Sci. Technol. Int. J.* **2019**, 22, 538–547. [CrossRef]
- 17. Avatar, K.; Mazumdar, D. Numerical Modeling of Melt Flow and Mixing in an Inductively Stirred Ladle and Comparison with Gas and Mechanical Stirring. *Steel Res. Int.* **2024**, 2300711. [CrossRef]
- 18. Bai, K.; Katz, J. On the refractive index of sodium iodide solutions for index matching in PIV. Exp. Fluids 2014, 55, 1–6. [CrossRef]
- 19. Haas, T.; Suarez, A.L.; Eickhoff, M.; Pfeifer, H. Toward a strong-sense validation benchmark database for numerical ladle flow models. *Metall. Mater. Trans. B* **2021**, *52*, 199–222. [CrossRef]
- 20. Conejo, A.N. Fundamentals of Dimensional Analysis: Theory and Applications in Metallurgy; Springer Nature: New York, NY, USA, 2021.
- 21. Mazumdar, D. On the estimation of plume rise velocity in gas-stirred ladles. Met. Mater. Trans. B 2002, 33, 937–941. [CrossRef]
- 22. Mietz, J.; Schneider, S.; Oeters, F. Model experiments on mass transfer in ladle metallurgy. Steel Res. 1991, 62, 1–9. [CrossRef]
- 23. Li, L.; Liu, Z.; Li, B.; Matsuura, H.; Tsukihashi, F. Water Model and CFD-PBM Coupled Model of Gas-Liquid-Slag Three-Phase Flow in Ladle Metallurgy. *ISIJ Int.* **2015**, *55*, 1337–1346. [CrossRef]
- 24. Zhang, H.; Lei, H.; Ding, C.; Chen, S.; Xiao, Y.; Li, Q. Two-Way PBM–Euler Model for Gas and Liquid Flow in the Ladle. *Materials* 2023, *16*, 3782. [CrossRef] [PubMed]
- 25. Lou, W.; Zhu, M. Numerical Simulation of Gas and Liquid Two-Phase Flow in Gas-Stirred Systems Based on Euler–Euler Approach. *Met. Mater. Trans. B* **2013**, *44*, 1251–1263. [CrossRef]
- Laux, H.; Johansen, S.T. A CFD analysis of the air entrainment rate due to a plunging steel jet combining mathematical models
  for dispersed and separated multiphase flows. In *Fluid Flow Phenomena in Metals Processing*; TMS Publisher: Pittsburgh, PA, USA,
  1999; pp. 21–30.
- 27. Cloete, S.; Olsen, J.E.; Skjetne, P. CFD modeling of plume and free surface behavior resulting from a sub-sea gas release. *Appl. Ocean Res.* **2009**, *31*, 220–225. [CrossRef]
- 28. Konno, M.; Arai, K.; Saito, S. The effects of viscous and inertial forces on drop breakup in an agitated tank. *J. Chem. Eng. Jpn.* 1977, 10, 474–477. [CrossRef]
- 29. Konno, M.; Matsunaga, Y.; Arai, K.; Saito, S. Simulation model for breakup process in an agitated tank. *J. Chem. Eng. Jpn.* **1980**, *13*, 67–73. [CrossRef]
- 30. Tennekes, H.; Lumley, J.L. A First Course in Turbulence; MIT Press: Cambridge, MA, USA, 1972.
- 31. Pope, S.B. *Turbulent Flows*; Cambridge University Press: Cambridge, UK, 2000.
- 32. Swanson Analysis Systems, Inc. ANSYS Fluent Theory Guide 15.0; ANSYS: Canonsburg, PA, USA, 2013; p. 33.
- 33. Hinze, J.O. Turbulence; McGraw-Hill Publishing, Co.: New York, NY, USA, 1975.
- 34. Jojo-Cunningham, Y.; Guo, X.; Zhou, C.; Liu, Y. Volumetric Flow Field inside a Gas Stirred Cylindrical Water Tank. *Fluids* **2023**, *9*, 11. [CrossRef]
- 35. Schanz, D.; Gesemann, S.; Schröder, A. Shake-The-Box: Lagrangian particle tracking at high particle image densities. *Exp. Fluids* **2016**, *57*, 70. [CrossRef]
- 36. Novara, M.; Schanz, D.; Schröder, A. Two-Pulse 3D particle tracking with Shake-The-Box. Exp. Fluids 2023, 64, 93. [CrossRef]
- 37. Li, Q.; Pistorius, P.C. Large Bubble-Resolved Direct Numerical Simulation for Multiphase Flow Applied to Gas-Stirred Ladles: Grid Resolution and Plug Eccentricity Effects. *Met. Mater. Trans. B* **2023**, *54*, 1290–1313. [CrossRef]
- 38. Duruiheme, O.Q.; Guo, X.; Walla, N.; Zhou, C. Dissolution of Microalloying Elements in a Ladle Metallurgy Furnace. *Metals* **2023**, 13, 421. [CrossRef]
- 39. Zhou, X.; Zhang, Y.; He, Q.; Ni, P.; Yue, Q.; Ersson, M. Novel Evaluation Method to Determine the Mixing Time in a Ladle Refining Process. *Met. Mater. Trans. B* **2022**, *53*, 4114–4123. [CrossRef]

**Disclaimer/Publisher's Note:** The statements, opinions and data contained in all publications are solely those of the individual author(s) and contributor(s) and not of MDPI and/or the editor(s). MDPI and/or the editor(s) disclaim responsibility for any injury to people or property resulting from any ideas, methods, instructions or products referred to in the content.